Research Article | Vol. 27, No. 4 | 18 Feb 2019 | OPTICS EXPRESS A133
Optics EXPRESS

Efficient wave optics modeling of nanowire solar cells using rigorous coupled-wave analysis

KYLE W. ROBERTSON,[1] RAY R. LAPIERRE,[2] AND JACOB J. KRICH[1,3,*]

[1]Department of Physics, University of Ottawa, Ottawa, Ontario K1N 6N5, Canada
[2]Department of Engineering Physics, McMaster University, Hamilton, Ontario L8S 4L7, Canada
[3]School of Electrical Engineering and Computer Science, University of Ottawa, Ottawa, Ontario K1N 6N5, Canada
[*]jkrich@uottawa.ca

Abstract: We investigate the accuracy of rigorous coupled-wave analysis (RCWA) for near-field computations within cylindrical GaAs nanowire solar cells and discover excellent accuracy with low computational cost at long incident wavelengths but poor accuracy at short incident wavelengths. These near fields give the carrier generation rate, and their accurate determination is essential for device modeling. We implement two techniques for increasing the accuracy of the near fields generated by RCWA and give some guidance on parameters required for convergence along with an estimate of their associated computation times. The first improvement removes Gibbs phenomenon artifacts from the RCWA fields, and the second uses the extremely well-converged far-field absorption to rescale the local fields. These improvements allow a computational speedup between 30 and 1000 times for spectrally integrated calculations, depending on the density of the near fields desired. Some spectrally resolved quantities, especially at short wavelengths, remain expensive, but RCWA is still an excellent method for performing those calculations. These improvements open up the possibility of using RCWA for low-cost optical modeling in a full optoelectronic device model of nanowire solar cells.

1. Introduction

Nanowire solar cells (NWSC) are a new solar cell technology with the potential to improve upon existing solar cell devices. Their potential stems from their ability to effectively absorb incident light while using less semiconductor material than planar solar cells.

The optimal nanowire solar cell arrays consists of nanowires that are a few microns in height and with diameters and periodicities comparable to the wavelengths present in the solar spectrum [1, 2]. These small sizes require full wave optics simulations to accurately model their optical properties, unlike in standard planar devices [3, 4]. Both experimental measurements and modeling have shown high levels of absorption with low sensitivity to the incident angle of light [5]. Additionally, the finite in-plane dimensions of nanowires can accommodate strain due to growth on lattice-mismatched substrates without introducing dislocation faults in the crystal lattice [6]. This capability opens up the possibility for high-efficiency III-V tandem cells grown on silicon [7].

The larger design parameter space of NWSC relative to planar solar cells requires careful optimization of geometric parameters to maximize device performance [8]. There is a need for fast, accurate modeling tools to enable rapid exploration and optimization of nanowire designs. Conventionally, finite element [4, 9–11] and finite difference methods [1, 12, 13] have been used in optical models of NWSC. While these techniques are highly accurate, they are computationally expensive, limiting their usefulness in a closed-loop global device optimization. Rigorous

#349636 https://doi.org/10.1364/OE.27.00A133
Journal © 2019 Received 31 Oct 2018; revised 21 Dec 2018; accepted 30 Dec 2018; published 6 Feb 2019

coupled-wave analysis (RCWA) is another wave-optics modeling technique that lacks the memory and computational requirements of competing techniques [14]. RCWA is a Fourier domain technique ideally suited to periodic arrays. It is promising for its speed and is highly accurate when computing far-field quantities such as total absorptance, reflectance, and transmittance. RCWA simulations become more accurate as the number of plane waves N_G increases, and the computational cost scales as N_G^3. However, naive implementations lack accuracy at reasonable N_G when computing near-fields internal to the device due to the well-known Gibbs phenomenon [15]. Such near-fields are required to compute carrier generation rates and are thus an essential component of a fully-coupled optoelectronic device model.

In this work, we show that RCWA can be used for accurate optical modeling of nanowire solar cells. We examine a test device (see Fig. 1 and Table 1), indicate where standard RCWA formulations lack sufficient accuracy, and provide two techniques for increasing accuracy of the near fields. The first is an implementation of an already published technique for introducing proper discontinuities in the near fields and mitigating the Gibbs phenomenon [15–18]. We extend the open source RCWA library S^4 to include this technique, and show it greatly increases the accuracy of local field computations [19]. The second is a new rescaling technique that increases the accuracy of device simulations while keeping computational cost reasonable when computing spectrally integrated quantities. We show that even with our two improvements, some spectrally resolved quantities continue to require more expensive calculations. Using our improvements, RCWA shows promise as an effective technique for rapid optical modeling of nanowire solar cells.

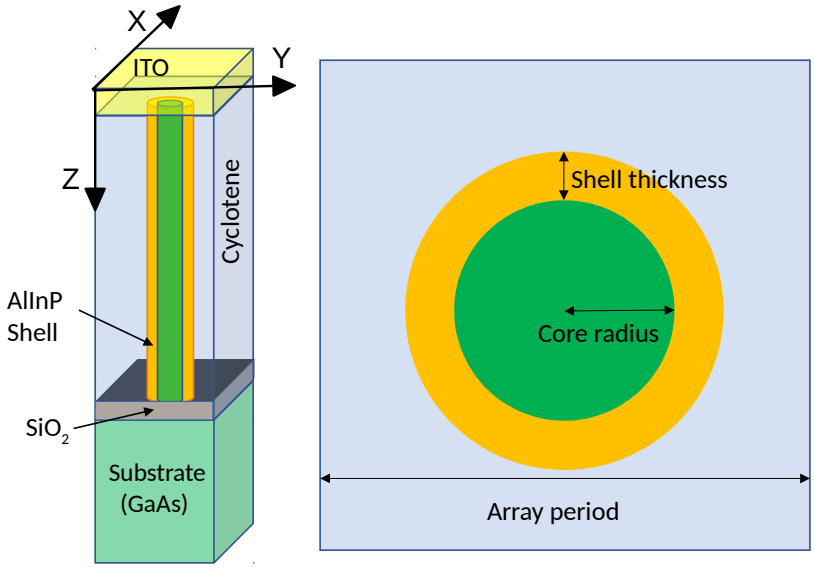

Fig. 1. The test device used for assessment of RCWA. Left: A single unit cell in a square nanowire array containing a cylindrical GasAs nanowire passivated by an AlInP shell on a GaAs substrate, planarized by a cyclotene dielectric, and top-contacted with a layer of indium tin oxide. A thin layer of SiO_2, surrounding the GaAs core but lacking the AlInP shell, exists between the cyclotene and substrate. Right: A top down view of the unit cell, demonstrating the piecewise constant material parameters in the plane.

Optics EXPRESS

Table 1. Numerical values for all geometric parameters in the test device.

Parameter	Value
NW Core Length	1.3 μm
NW Shell Length	1.27 μm
SiO_2 Thickness	30 nm
Substrate Thickness	1 μm
ITO Thickness	300 nm
Array Period	250 nm
Core Radius	60 nm
Shell Thickness	20 nm

2. RCWA

RCWA is a Fourier-space method for solving the frequency domain Maxwell's equations with frequency ω:

$$\nabla \times \mathbf{H} = -i\omega\epsilon\mathbf{E} + \mathbf{J}_f \tag{1}$$
$$\nabla \times \mathbf{E} = i\omega\mu\mathbf{H} \tag{2}$$
$$\nabla \cdot \mathbf{B} = 0 \tag{3}$$
$$\nabla \cdot \mathbf{D} = \rho_f \tag{4}$$

where $\mathbf{B} = \mu\mathbf{H}$ is the magnetic field, $\mathbf{E}$ is the electric field, $\mathbf{D} = \epsilon\mathbf{E}$ is the displacement field, ϵ is the electric permitivitty, μ is the magnetic permeability, $\mathbf{J}_f$ is the free current density, and ρ_f is the free charge density. RCWA relies on two critical assumptions about the geometry of the system. First, the device must be composed of discrete, axially-invariant layers such that at a given x-y point within a layer, the material parameters along the z-direction remain constant. Second, the device must be decomposable into fundamental unit cells that are 2D periodic in the plane. If these conditions are satisfied, then the longitudinal and transverse dimensions are separable and the fields in a single layer can be written as:

$$\mathbf{H}(\mathbf{r}, z) = \sum_{\mathbf{G}} \mathbf{H}_{\mathbf{G}}(z) e^{i(\mathbf{k}+\mathbf{G})\cdot\mathbf{r}}, \tag{5}$$

where $\mathbf{G}$ is one of N_G in-plane reciprocal lattice vectors, $\mathbf{k}$ is the in-plane component of the excitation wave vector, and $\mathbf{r} = x\hat{\mathbf{x}} + y\hat{\mathbf{y}}$. Note the $\mathbf{G}$ is generally chosen to be an array of reciprocal lattice points with a circular truncation, keeping all $\mathbf{G}$ with $|\mathbf{G}|$ less than some constant, which maintains symmetry in Fourier space [19]. The in-plane dielectric profile $\epsilon(\mathbf{r})$ may depend on the material, allowing it to have piecewise-constant dependence on the transverse spatial coordinates. Vertical nanowire arrays (see Fig. 1) satisfy these geometric constraints.

We consider only non-magnetic materials, so $\mu = \mu_0$, the vacuum permeability. At optical frequencies, which we consider, ρ_f is negligible. $\mathbf{J}_f$ can be used to describe emission from within structures; we will not make such considerations and will thus consider $\mathbf{J}_f = 0$ in the examples below, but such currents could be added without difficulty.

The approximation of step changes in ϵ, while convenient mathematically, is known to produce singularities in local fields and their gradients at internal corners and edges [20]. These

singularities are square integrable, as is required for conservation of energy, but are generally not fully resolvable with standard FDTD, FEM, and RCWA methods, though specialized methods have been proposed to treat some of the singularities in particular geometries [21–23]. The cylindrical geometry considered here contains no corners and the active region of GaAs is convex, so the field singularities inside the nanowire material are relatively benign, but they are not accurately modeled here. Instead, we effectively spread the associated optical generation over a region given by the Fourier resolution, which scales as the unit cell period divided by $\sqrt{N_G}$. Since this length scale is smaller than material diffusion lengths, we do not anticipate effects in device modeling.

The essential part of RCWA is determining $\mathbf{H}_\mathbf{G}(z)$ in Eq. (5) for a given set of reciprocal lattice vectors $\mathbf{G}$. One can assume the coefficients in Eq. (5) take the form [19]

$$\mathbf{H}_\mathbf{G}(z) = \left[\phi_{\mathbf{G},x}\hat{\mathbf{x}} + \phi_{\mathbf{G},y}\hat{\mathbf{y}} - \frac{(k_x + G_x)\phi_{\mathbf{G},x} + (k_y + G_y)\phi_{\mathbf{G},y}}{q}\hat{\mathbf{z}}\right] e^{iqz}, \tag{6}$$

where the ϕ are expansion coefficients and the z-component has been chosen to satisfy the $\nabla \cdot \mathbf{H} = 0$ condition. This form of the fields illustrates one of the key advantages of RCWA over competing techniques, namely the analytic dependence on the z coordinate. By inserting Eq. (6) into Eq. (1), one arrives at an eigenvalue equation for determining the set of eigenvalues q and the components of the eigenvectors ϕ for a single layer. Once the eigenmodes of each layer have been determined, multilayer structures are joined together by introducing propagation amplitudes for the eigenmodes and using the scattering matrix method to join solutions at layer interfaces [24–28]. Results increase in accuracy with N_G. Our work is an extension to S^4, an open-source implementation of RCWA built on the scattering matrix method [19]. In the remainder of the manuscript, we refer to S^4 as the standard RCWA method, but it has included a significant number of improvements from the original RCWA methods; for details, see [19].

For optoelectronic device modeling, we are most concerned with determining the local carrier generation rate, which is determined from the local electric field strength in each material. RCWA expresses the fields using the Fourier series in Eq. (5). Any finite Fourier series representation is always continuous, even across in-plane material interfaces, as between the core and shell of a nanowire. In an exact solution, the normal components of $\mathbf{E}$ should be discontinuous across material boundaries, but a Fourier reconstruction requires an intractable number of terms to accurately model such a discontinuity, even though far-field quantities such as the total absorptance may be well converged. For any finite N_G, standard RCWA-produced fields have spurious oscillations, especially near material interfaces.

To assess the convergence of RCWA with N_G, we define two methods for computing the absorptance of a layer of the device. The first method relies only on the power passing through the top and bottom of the layer. These powers can be computed entirely in Fourier space [19], and do not suffer from convergence issues in the reconstruction of the near fields. The net emitted powers of layer i are defined as:

$$P^i_{\text{up}}(\omega) = \int_{\text{top}} S_z(\omega) dA \tag{7}$$

$$P^i_{\text{down}}(\omega) = \int_{\text{bottom}} S_z(\omega) dA, \tag{8}$$

where S_z is the z-component of the Poynting vector and the integration is over the top or bottom surface of the unit cell, with the appropriate sign for emitted power. Considering the top (layer 1) and bottom (layer n) together, the total reflectance and transmittance are

Optics EXPRESS

$$R(\omega) = \frac{P^1_{\text{up}}(\omega)}{P_{\text{in}}(\omega)} \tag{9}$$

$$T(\omega) = \frac{P^n_{\text{down}}(\omega)}{P_{\text{in}}(\omega)}, \tag{10}$$

where P_{in} is the input power of the incident plane wave. Then total absorptance is:

$$A_{\text{far field}}(\omega) = 1 - R(\omega) - T(\omega). \tag{11}$$

The contribution of a single layer to the device absorptance can be calculated similarly. We consider the test structure detailed in Table 1 and use S^4 [19] to perform RCWA calculations with normally-incident circularly polarized light. Due to the circular symmetry of the nanowires, total absorption is independent of the handedness of the incident light, so we can consider just one polarization and determine the local field strengths even for incoherent illumination [11]. We consider 60 equally spaced frequencies corresponding to wavelengths from 300 nm to 900 nm, just beyond the GaAs absorption edge of 871 nm. Figure 2 shows that the far-field absorptance spectrum of the full device converges rapidly with basis terms, and is self-converged within 0.5% with $N_G = 75$.

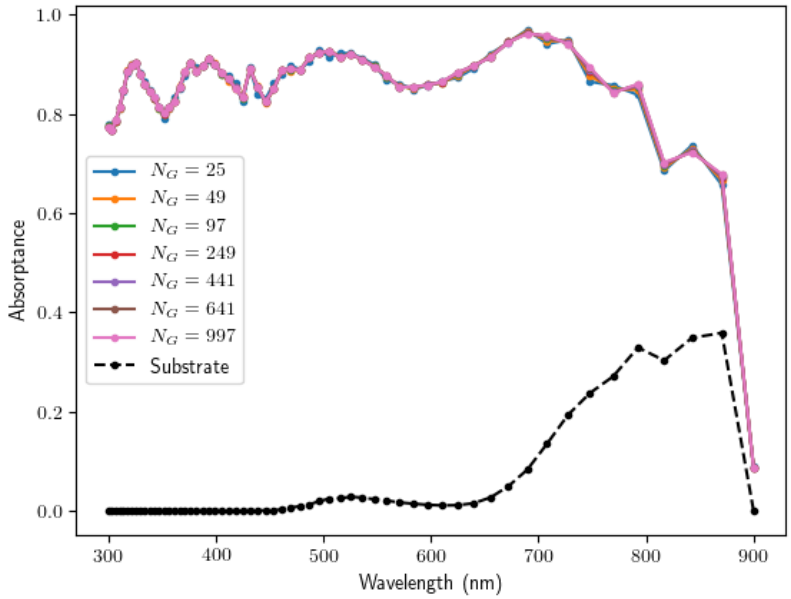

Fig. 2. Absorptance of the entire device calculated using the far field fluxes, Eqs. (7) - (11). The markers for all values of N_G lie nearly on top of one another, indicating convergence at low numbers of basis terms. The dashed black line shows the portion of the absorptance that occurs in the GaAs substrate (calculated with $N_G = 997$), which is negligible at shorter wavelengths, becoming more significant at longer wavelengths.

Equation (11) expresses the power absorbed in a layer in terms of the fluxes into and out of the layer. The divergence theorem and Maxwell's equations allow rewriting that power in terms of the local fields, instead. The absorbed power can then be written,

$$\mathcal{P}_{\text{abs}}(\omega) = \epsilon_0 \omega \int n(x, y, z; \omega) k(x, y, z; \omega) |E(x, y, z; \omega)|^2 dV \tag{12}$$

$$A_{\text{near field}} = \frac{\mathcal{P}_{\text{abs}}}{P_{\text{in}}}. \tag{13}$$

The complex dielectric at each frequency is constructed from tabulated real n and imaginary k

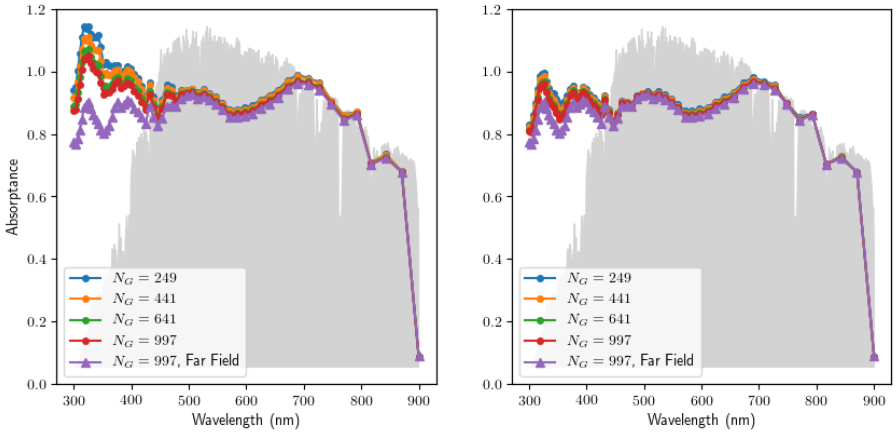

Fig. 3. Absorptance calculated from near fields using Eqs. (12) - (13) (circles). Far field absorptance at $N_G = 997$ (triangles). a) S^4 implementation of RCWA. b) Continuous variable formulation. Gray background shows the AM1.5 solar spectrum. The CVF shows significant improvement, especially at short wavelengths.

parts of the index of refraction in each material [9, 29].

We calculate $A_{\text{near field}}$ by extracting $\mathbf{E}(\mathbf{r})$ on a cubic mesh with 1 nm spacing in the plane for all layers. We use 3 nm spacing along the z-direction in the ITO layer and 3.5 nm spacing in the nanowire layer. A sparser mesh of 16 nm spacing is used in the substrate due to the weak absorption there. This choice of mesh is sufficiently dense to converge the result better than 1% using a simple trapezoidal rule integration. Figure 3(a) shows the convergence of $A_{\text{near field}}$ with N_G. Though the near fields are well converged for $\lambda > 450$ nm, they are not converged at short wavelengths even for $N_G = 997$.

Figure 4 shows some results of Figs. 2 and 3 as a function of N_G at three wavelengths and spectrally integrated with the AM1.5G solar spectrum [32], to more clearly show that the far-field method (green line) converges rapidly at all wavelengths, while the standard local-field method (blue line) only converges to the far-field result for long wavelength.

In the following sections, we provide two techniques for improving the accuracy of the near fields in RCWA. The first is an implementation of an existing technique, which we call the continuous variable formulation (CVF), which mitigates the Gibbs phenomenon and ensures proper discontinuities at interfaces by modifying the field computations such that only quantities that are continuous in real space are reconstructed from their Fourier components [15]. The discontinuities across in-plane material boundaries are then handled in real space. The second technique uses the well-converged, highly accurate far-field computation of each layer's absorption to rescale the near fields, ensuring correct total generation within a device layer.

Optics EXPRESS

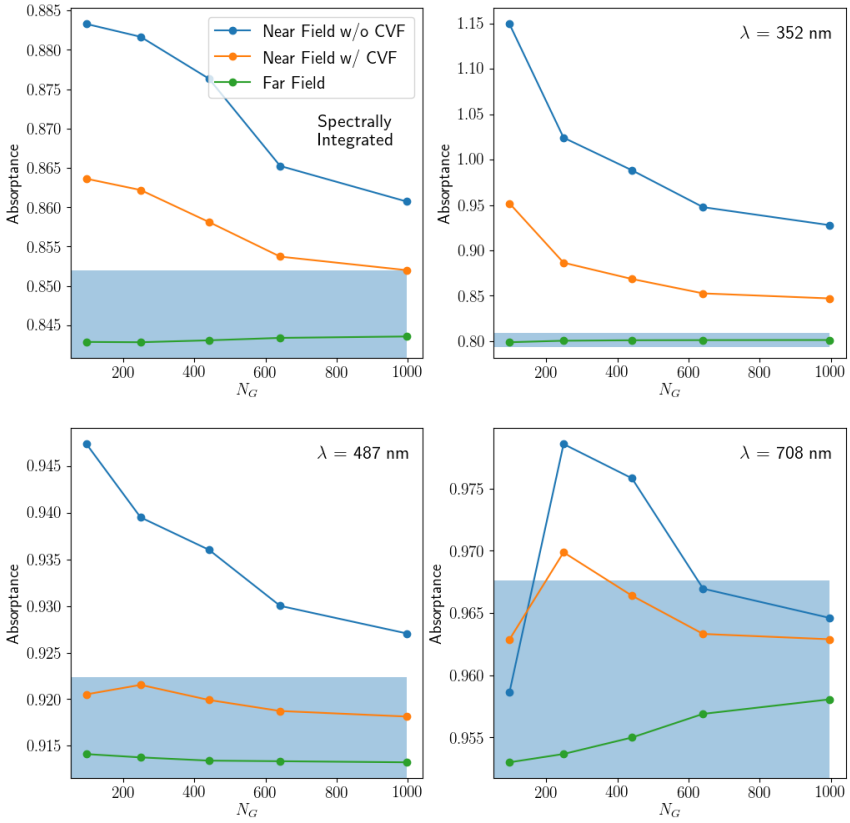

Fig. 4. Convergence of the spectrally integrated and wavelength resolved $A_{\text{far field}}$, $A_{\text{near field}}$ using the CVF fields, and $A_{\text{near field}}$ using the unmodified fields. Blue box indicates 1% error bars around the $N_G = 997$ far field absorptance, showing that the far field absorptance is self-converged in all cases; at short wavelengths, neither near field absorptance line is converged. The CVF fields improve accuracy at all wavelengths.

3. Continuous variable formulation

The CVF is a modification to RCWA that only Fourier reconstructs quantities that are continuous across material interfaces in real space. Near material interfaces, these quantities are the components of the displacement field $\mathbf{D}$ that are normal to, and the components of the electric field $\mathbf{E}$ that are tangential to, the interface. Using these real-space continuous quantities, one can determine the full electric field everywhere by using the constitutive relationship

$$\mathbf{D} = \epsilon \mathbf{E} \tag{14}$$

with a discontinuous real-space ϵ. S^4 already uses a related technique for calculating the Fourier modes, but it does not use this method when extracting real-space quantities.

To perform this decomposition with arbitrarily shaped 2D regions within a layer, one must construct a locally-defined vector field that is tangent to all material interfaces and periodic in the plane, which can be generated automatically, as is done by S^4 [19, 30]. This vector field induces an associated projection operator T that can be used to project the Cartesian components of the electromagnetic fields onto this local coordinate system such that:

$$\begin{bmatrix} E_{T,x}(\mathbf{r}) \\ E_{T,y}(\mathbf{r}) \end{bmatrix} = T(\mathbf{r}) \begin{bmatrix} E_x(\mathbf{r}) \\ E_y(\mathbf{r}) \end{bmatrix} \tag{15}$$

$$\begin{bmatrix} D_{N,x}(\mathbf{r}) \\ D_{N,y}(\mathbf{r}) \end{bmatrix} = N(\mathbf{r}) \begin{bmatrix} D_x(\mathbf{r}) \\ D_y(\mathbf{r}) \end{bmatrix}, \tag{16}$$

where $N = 1 - T$, $\mathbf{E}_T$ is the component of $\mathbf{E}$ along the tangential vector field and $\mathbf{D}_N$ is the component of $\mathbf{D}$ perpendicular to the tangential vector field. The total field satisfies

$$\begin{bmatrix} E_x(\mathbf{r}) \\ E_y(\mathbf{r}) \end{bmatrix} = \begin{bmatrix} E_{T,x}(\mathbf{r}) \\ E_{T,y}(\mathbf{r}) \end{bmatrix} + \begin{bmatrix} E_{N,x}(\mathbf{r}) \\ E_{N,y}(\mathbf{r}) \end{bmatrix}. \tag{17}$$

By taking the Fourier transform of $T(\mathbf{r})$, the projection onto the tangential vector field can also be done in Fourier space. Mirroring the notation of [15], we denote discrete real-space quantities with upper case letters (as in E_x to represent the vector $E_x(\mathbf{r}_i)$ for many points $\mathbf{r}_i$), vectors of Fourier coefficients with lower case letters surrounded by single brackets (as in $[e_x]$), and Fourier space matrix operators with double brackets (as in $[\![T]\!]$). Using this notation, the Fourier transform of Eq. (15) is given by [15]:

$$\begin{bmatrix} e_{T,x} \\ e_{T,y} \end{bmatrix} = [\![T]\!] \begin{bmatrix} e_x \\ e_y \end{bmatrix}, \tag{18}$$

where $[\![T]\!]$ is the Fourier convolution matrix [15,19]. That is, one calculates the Fourier transform $\tilde{T}(\mathbf{G})$ of $T(\mathbf{r})$, and the $(\mathbf{G}, \mathbf{G}')$ element of $[\![T]\!]$ is $\tilde{T}(\mathbf{G} - \mathbf{G}')$.

We extract $[e_x]$ and $[e_y]$ from a standard RCWA implementation and then construct $[d_{N,x}]$ and $[d_{N,y}]$. Since $\epsilon(\mathbf{r})$ and $\mathbf{E}_N(\mathbf{r})$ are both discontinuous, the proper Fourier factorization takes [31]

$$\left[\!\!\left[\frac{1}{\epsilon}\right]\!\!\right]^{-1} [\mathbf{d}_N] = [\mathbf{e}_N], \tag{19}$$

where $[\![1/\epsilon]\!]^{-1}$ is the $2N_G \times 2N_G$ block diagonal matrix whose upper-left and lower-right blocks are the inverse of the $N_G \times N_G$ Fourier convolution matrix of $1/\epsilon(\mathbf{r})$. In [15], Weismann et al. showed that the symmetric formulation,

$$\begin{bmatrix} d_{N,x} \\ d_{N,y} \end{bmatrix} = \frac{1}{2} \left([\![N]\!] \left[\!\!\left[\frac{1}{\epsilon}\right]\!\!\right]^{-1} + \left[\!\!\left[\frac{1}{\epsilon}\right]\!\!\right]^{-1} [\![N]\!] \right) \begin{bmatrix} e_x \\ e_y \end{bmatrix}, \tag{20}$$

converges well and conserves power for lossless structures, and we use this form.

After finding $d_{N,x}$ and $d_{N,y}$ we reconstruct the real space electric field

$$\mathbf{E}_N(\mathbf{r}) = \frac{\mathcal{F}^{-1}(\mathbf{d}_N)}{\epsilon_0 \epsilon_r(\mathbf{r})}, \tag{21}$$

where $\mathcal{F}^{-1}$ indicates the inverse Fourier transform. This $\mathbf{E}_N(\mathbf{r})$ has correct discontinuities at material interfaces where ϵ_r jumps. Finally, the real space electric fields in Cartesian coordinates can be recovered using:

Optics EXPRESS

$$E_y(\mathbf{r}) = \frac{\mathcal{F}^{-1}(d_{N,y})}{\epsilon_0 \epsilon_r(\mathbf{r})} + \mathcal{F}^{-1}(e_{T,y}) \tag{22}$$

$$E_x(\mathbf{r}) = \frac{\mathcal{F}^{-1}(d_{N,x})}{\epsilon_0 \epsilon_r(\mathbf{r})} + \mathcal{F}^{-1}(e_{T,x}). \tag{23}$$

Figure 5 shows the norm-squared components of the electric fields computed using unmodified RCWA and the CVF on a line cut along the x-direction through the center of the nanowire. In this cut, E_x is normal to the interface and should therefore be discontinuous, while E_y should be continuous. Note the Gibbs oscillations in the standard result for E_x, while the CVF result has introduced discontinuities at the boundaries and significantly reduced the amplitude of the Gibbs oscillations.

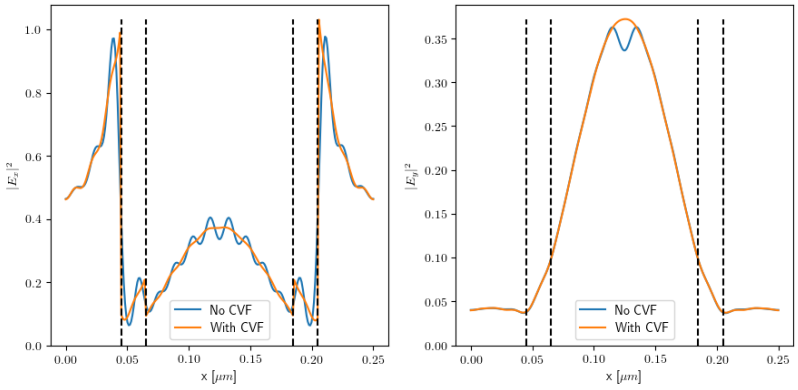

Fig. 5. Line cuts of $|E_x|^2$ (left) and $|E_y|^2$ (right) along the x-direction through the center of the nanowire 101 nm from the top of the nanowire with and without use of the CVF with an incident wavelength of 453 nm and N_G = 997. The CVF formulation reduces the Gibbs oscillations in E_x and introduces proper discontinuities while maintaining the continuity of E_y.

Figure 3(b) shows the improved agreement between the CVF absorptance and the well-converged far field absorptance. Figure 6 shows the relative difference between the far and near field absorptances calculated with and without the CVF. It is clear that the CVF significantly improves the agreement at all wavelengths, but the disagreement is still significant for wavelengths shorter than 450 nm. Figure 6 indicates the AM1.5G spectrum, which shows that the CVF-based $A_{\text{near field}}$ agrees well with the far field results through the most important parts of the solar spectrum. In the next section, we introduce a simple rescaling technique to increase accuracy of the near fields at all incident wavelengths.

4. Rescaling technique

In device simulations, the total optical generation rate must be determined accurately. The exact position where generation occurs is somewhat less important, as the carriers drift and diffuse, and deviations on the scale of a few nanometers are rarely significant. We can ensure that the total generation in each layer is calculated correctly, even with inexpensive RCWA calculations that have not fully converged the local fields. To achieve this goal, we use the well-converged far field results (as shown in Fig. 2) to rescale the components of the near fields in each layer such that $A_{\text{far field}}$ and $A_{\text{near field}}$ agree exactly. We define a rescaling factor F for each layer i and frequency ω:

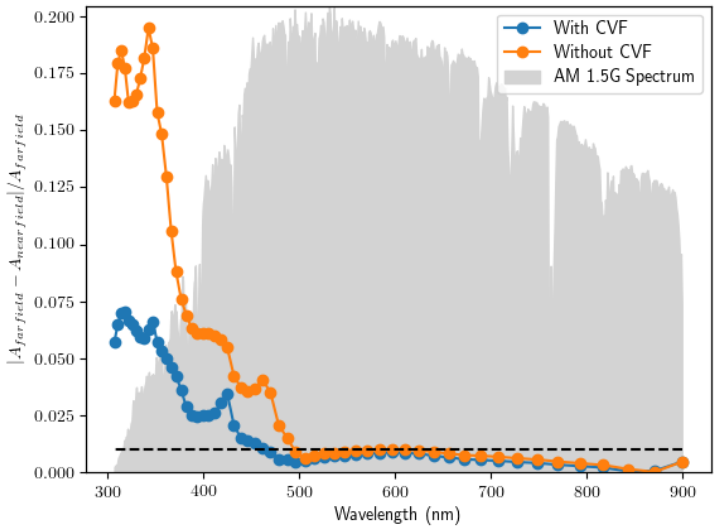

Fig. 6. Relative difference between the far field and near field calculations of A with $N_G = 997$. Orange line uses the unmodified fields in Eq. 13, blue line uses the CVF fields. Gray background shows the AM1.5G solar spectrum, which is strongest in the region of good convergence. Black dashed line indicates the 1% mark.

$$F_i(\omega) = \frac{A^i_{\text{far field}}(\omega)}{A^i_{\text{near field}}(\omega)}. \tag{24}$$

Then, the components of $\mathbf{E}$ are rescaled such that:

$$\mathbf{E}^{\text{rescaled}}(\omega) = \sqrt{F_i(\omega)}\mathbf{E}(\omega) \tag{25}$$

for fields in the appropriate layer, ensuring that the total generation rate in each layer matches the accurate far-field result exactly.

This rescaling technique allows accurate determination of spectrally-integrated generation rates with small numbers of basis terms. Figures 7 and 8 show line cuts through the test structure at three representative wavelengths and spectrally integrated under AM1.5G illumination, calculated with 60 equally spaced frequencies. At 487 nm, the fields are quantitatively converged at small N_G, while the Gibbs oscillations are not entirely removed either at shorter or longer wavelengths. Calculations dependent on spectrally resolved local fields, such as external quantum efficiency (EQE), thus require relatively large N_G at some wavelengths. When the fields are spectrally integrated, however, the essentially random phases of the oscillations average away, and the spectrally-integrated fields are quantitatively converged by $N_G = 197$. Figure 9 compares the rescaled spectrally-integrated generation rates along a plane through the center of the nanowire at $N_G = 997$ and 197, showing the excellent agreement that rescaling permits, even at low N_G. This spectrally integrated generation rate is sufficient for optoelectronic modeling while reducing the requirements for N_G by a factor of 5.

The computational cost of the RCWA method scales as N_G^3, so reducing N_G by a factor of 5 (from 1000 to 200) theoretically reduces the runtime by a factor of 125, and reducing to $N_G = 100$ can reduce the runtime by a factor of 1000. Extracting the electric fields on a dense mesh of

Optics EXPRESS

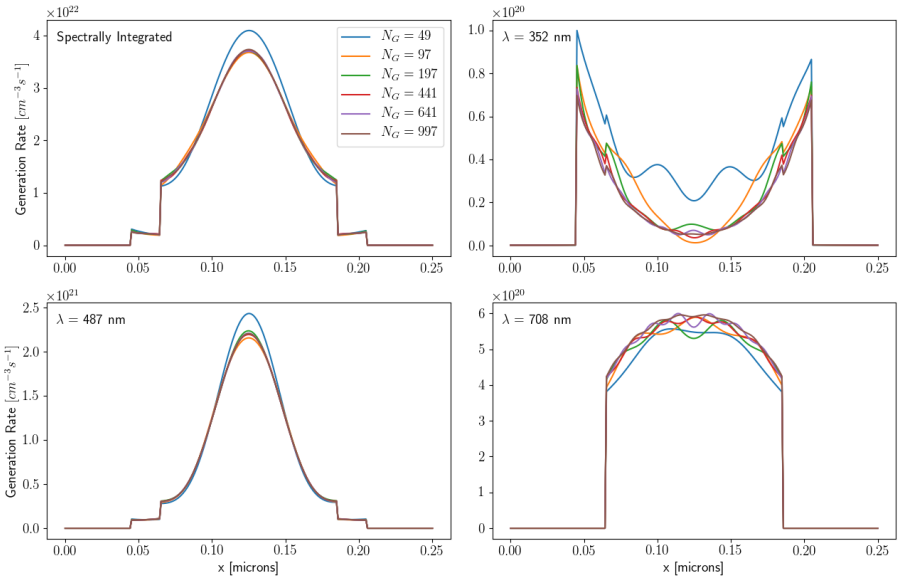

Fig. 7. Rescaled generation rate on a line cut along the x direction through the center of the nanowire 83 nm from the top of the nanowire layer. The spectrally integrated and $\lambda = 487$ nm case are clearly converged even at $N_G = 197$, while the longer and shorter wavelengths need high N_G to remove all the Gibbs oscillations.

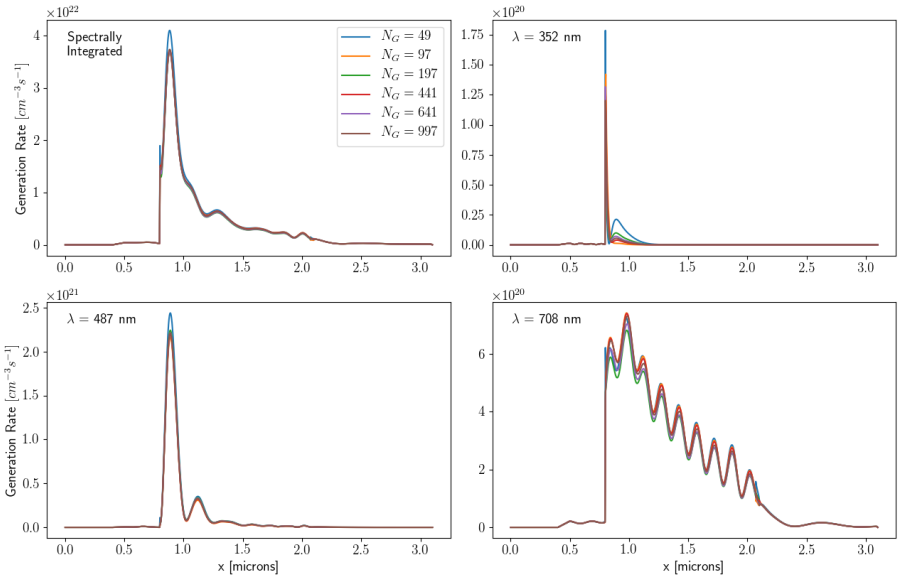

Fig. 8. Rescaled generation rate on a line cut along the z direction through the center of the nanowire core. As in Fig. 7, the spectrally integrated results are well converged at low N_G while the shortest and longest wavelengths require higher N_G for convergence.

Optics EXPRESS

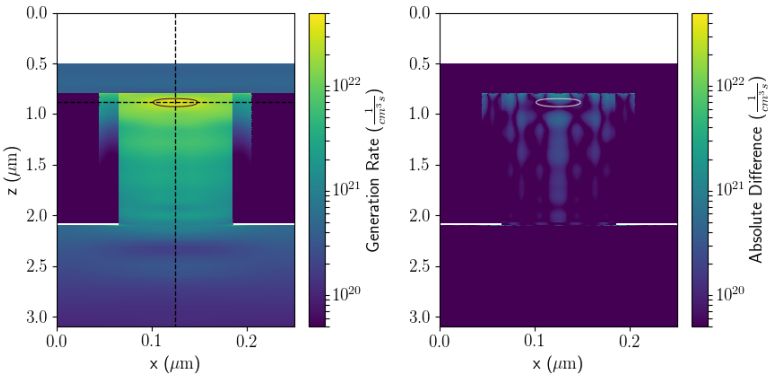

Fig. 9. Left: Spectrally integrated generation rate with AM1.5G spectrum along a cut through the middle of the nanowire using the rescaled fields with $N_G = 197$. Right: Absolute difference between the generation rate shown at left and the well-converged, rescaled generation rate at $N_G = 997$. The deviations between the two generation maps are small. White regions are areas of vacuum and SiO_2, where the generation rate is zero. Area within the solid contour indicates the location of peak generation, greater than 2.75×10^{22} cm^{-3}s^{-1}, while the differences there are much smaller. Dashed lines indicate line cuts shown in Figs. 7 and 8.

points, however, also has a computational cost, and for sufficiently small N_G, this electric-field extraction limits the runtime. Figure 10 shows an estimate of the simulation run times for a single incident wavelength. Each desired wavelength must be calculated separately, and they all take approximately the same amount of processor time. Simulations were run on a single core of an Intel Xeon E5-2640 v4 CPU with a 2.40GHz clock speed. The figure shows both the simulation time for RCWA to determine the field amplitudes, in Fourier space, and for the extraction of those fields on the dense real-space mesh described above. The CVF method does not significantly change the run times. Efforts were made to minimize data input/output time and resource contention in all benchmarks. These results show that running at $N_G = 197$ has a cost 25 times less than at $N_G = 997$, and that cost is dominated by the field calculation and export. The field calculation and export time can possibly be optimized further and would certainly be reduced if a coarser mesh were requested. Decreasing that cost could allow computation times to be reduced by an additional factor of 5. Simulations at each frequency are completely independent, so computation time for a full spectral sweep can be easily reduced by running all frequencies in parallel [33]. With a sufficient number of CPU cores, a full spectral sweep can be run in the same clock time as a single simulation.

Optics EXPRESS

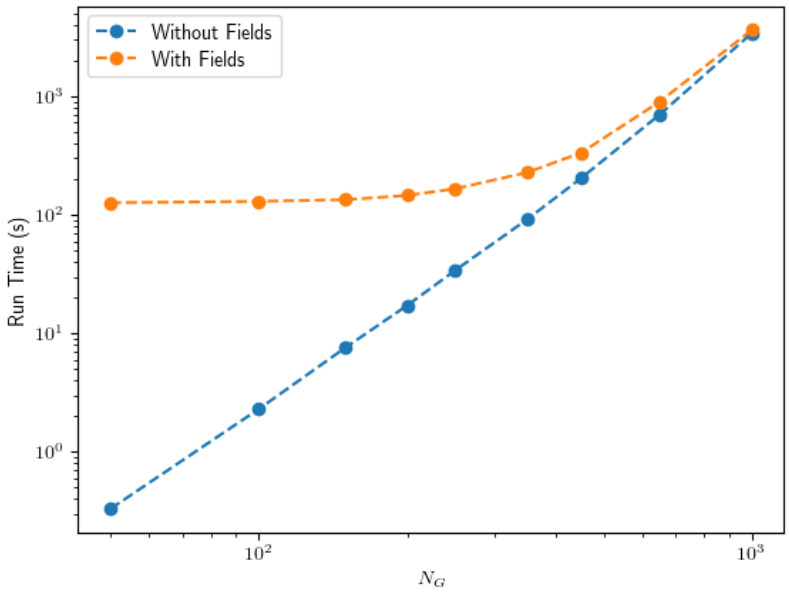

Fig. 10. Run time of a single simulation as a function of basis terms with and without computation of the local fields. Field computations dominate the runtime at small N_G. A least-squares fit to the blue line yields a slope of 3.06, consistent with the N_G^3 scaling of the QR algorithm for solving eigenvalue problems. Dashed lines are guides to the eye.

5. Conclusion

In this work, we investigate the accuracy of RCWA for optical modeling of nanowire solar cells. We find excellent accuracy with low computational cost at long incident wavelengths, but poor accuracy at short incident wavelengths. To increase the accuracy of RCWA we extend the open-source library S^4 [19] to include an already published technique for improving near field computations in RCWA [15]. Our implementation mitigates the Gibbs phenomenon and introduces physically expected discontinuities in the fields at material interfaces, improving convergence of the near fields at all incident wavelengths. To bring convergence within a 1% tolerance, we introduce a simple rescaling technique that uses the well converged far field quantities to rescale the near fields on a per layer basis. These improvements open up the possibility of using RCWA as a low cost optical modeling technique in a full optoelectronic device model of nanowire solar cells.

Funding

Natural Sciences and Engineering Research Council of Canada (STPGP 478768) and US Army Research Laboratory (W911NF-16-2-0167).

Acknowledgments

We thank Anna Trojnar for helpful conversations.

References

1. D. Wu, X. Tang, K. Wang, and X. Li, "An analytic approach for optimal geometrical design of GaAs nanowires for maximal light harvesting in photovoltaic cells," Sci. Reports **7**, 46504 (2017).

2. B. C. P. Sturmberg, K. B. Dossou, L. C. Botten, A. A. Asatryan, C. G. Poulton, R. C. McPhedran, and C. M. de Sterke, "Optimizing photovoltaic charge generation of nanowire arrays: A simple semi-analytic approach," ACS Photonics **1**, 683–689 (2014).
3. J. Wallentin, N. Anttu, D. Asoli, M. Huffman, I. Aberg, M. H. Magnusson, G. Siefer, P. Fuss-Kailuweit, F. Dimroth, B. Witzigmann, H. Q. Xu, L. Samuelson, K. Deppert, and M. T. Borgström, "InP nanowire array solar cells achieving 13.8% efficiency by exceeding the ray optics limit," Science **339**, 1057–1060 (2013).
4. J. Kupec, R. L. Stoop, and B. Witzigmann, "Light absorption and emission in nanowire array solar cells," Opt. Express **18**, 27589–27605 (2010).
5. O. M. Ghahfarokhi, N. Anttu, L. Samuelson, and I. Åberg, "Performance of GaAs nanowire array solar cells for varying incidence angles," IEEE J. Photovoltaics **6**, 1502–1508 (2016).
6. K. L. Kavanagh, "Misfit dislocations in nanowire heterostructures," Semicond. Sci. Technol. **25**, 024006 (2010).
7. M. T. Borgström, M. H. Magnusson, F. Dimroth, G. Siefer, O. Höhn, H. Riel, H. Schmid, S. Wirths, M. Björk, I. Åberg, W. Peijnenburg, M. Vijver, M. Tchernycheva, V. Piazza, and L. Samuelson, "Towards nanowire tandem junction solar cells on silicon," IEEE J. Photovoltaics **8**, 733–740 (2018).
8. K. W. Robertson, R. R. LaPierre, and J. J. Krich, "Optical optimization of passivated GaAs nanowire solar cells," in *2017 IEEE 44th Photovoltaic Specialist Conference* (IEEE, 2017), pp. 1294–1298.
9. Y. Hu, R. R. LaPierre, M. Li, K. Chen, and J.-J. He, "Optical characteristics of GaAs nanowire solar cells," J. Appl. Phys. **112**, 104311 (2012).
10. K. M. Azizur-Rahman and R. R. LaPierre, "Wavelength-selective absorptance in GaAs, InP and InAs nanowire arrays," Nanotechnology **26**, 295202 (2015).
11. A. H. Trojnar, C. E. Valdivia, R. R. LaPierre, K. Hinzer, and J. J. Krich, "Optimizations of GaAs nanowire solar cells," IEEE J. Photovoltaics **6**, 1494–1501 (2016).
12. K. T. Fountaine, W. S. Whitney, and H. A. Atwater, "Resonant absorption in semiconductor nanowires and nanowire arrays: Relating leaky waveguide modes to bloch photonic crystal modes," J. Appl. Phys. **116**, 153106 (2014).
13. Q. G. Du, C. H. Kam, H. V. Demir, H. Y. Yu, and X. W. Sun, "Broadband absorption enhancement in randomly positioned silicon nanowire arrays for solar cell applications," Opt. Lett. **36**, 1884–1886 (2011).
14. M. G. Moharam, T. K. Gaylord, E. B. Grann, and D. A. Pommet, "Formulation for stable and efficient implementation of the rigorous coupled-wave analysis of binary gratings," J. Opt. Soc. Am. A **12**, 1068–1076 (1995).
15. M. Weismann, D. F. Gallagher, and N. C. Panoiu, "Accurate near-field calculation in the rigorous coupled-wave analysis method," J. Opt. **17**, 125612 (2015).
16. P. Lalanne and M. P. Jurek, "Computation of the near-field pattern with the coupled-wave method for transverse magnetic polarization," J. Mod. Opt. **45**, 1357–1374 (1998).
17. K. H. Brenner, "Aspects for calculating local absorption with the rigorous coupled-wave method," Opt. Express **18**, 10369–10376 (2010).
18. E. A. Bezus and L. L. Doskolovich, "Stable algorithm for the computation of the electromagnetic field distribution of eigenmodes of periodic diffraction structures," J. Opt. Soc. Am. A **29**, 2307–2313 (2012).
19. V. Liu and S. Fan, "S4: A free electromagnetic solver for layered periodic structures," Comput. Phys. Commun. **183**, 2233–2244 (2012).
20. M. Costabel and M. Dauge, "Singularities of electromagnetic fields in polyhedral domains," Arch. for Ration. Mech. Analysis **151**, 221–276 (2000).
21. N. Huynh and W. Heinrich, "FDTD accuracy improvement by incorporation of 3D edge singularities," in *1999 IEEE MTT-S International Microwave Symposium Digest (Cat. No.99CH36282)* (IEEE, 1999), pp. 1573–1576.
22. A. Farjadpour, D. Roundy, A. Rodriguez, M. Ibanescu, P. Bermel, J. D. Joannopoulos, S. G. Johnson, and G. W. Burr, "Improving accuracy by subpixel smoothing in the finite-difference time domain," Opt. Lett. **31**, 2972–2974 (2006).
23. C. Epstein and M. O'Neil, "Smoothed corners and scattered waves," SIAM J. Sci. Comput. **38**, A2665–A2698 (2016).
24. L. Li, "Formulation and comparison of two recursive matrix algorithms for modeling layered diffraction gratings," J. Opt. Soc. Am. A **13**, 1024 (1996).
25. D. M. Whittaker and I. S. Culshaw, "Scattering-matrix treatment of patterned multilayer photonic structures," Phys. Rev. B **60**, 2610–2618 (1999).
26. M. G. Moharam and A. B. Greenwell, "Rigorous analysis of field distribution and power flow in grating coupler of finite length," in *Diffractive Optics and Micro-Optics,* (Optical Society of America, 2004), p. DMC5.
27. H. Kim, I. Lee, and B. Lee, "Extended scattering-matrix method for efficient full parallel implementation of rigorous coupled-wave analysis," J. Opt. Soc. Am. A **24**, 2313 (2007).
28. R. C. Rumpf, "Improved formulation of scattering matrices for semi-analytical methods that is consistent with convention," Prog. In Electromagn. Res. B **35**, 241–261 (2011).
29. S. Adachi, *Optical Constants of Crystalline and Amorphous Semiconductors: Numerical Data and Graphical Information* (Springer US, 1999), 1st ed.
30. P. Götz, T. Schuster, K. Frenner, S. Rafler, and W. Osten, "Normal vector method for the RCWA with automated vector field generation," Opt. express **16**, 17295–17301 (2008).
31. L. Li, "Use of Fourier series in the analysis of discontinuous periodic structures," J. Opt. Soc. Am. A **13**, 1870–1876 (1996).
32. "Standard tables for reference solar spectral irradiances: Direct normal and hemispherical on 37° tilted surface," Tech. rep., ASTM International (2012).

Optics EXPRESS

33. O. Tange, “Gnu parallel 2018,” https://doi.org/10.5281/zenodo.1146014 (2018).